

GT2011-46553

AERODYNAMIC CHARACTERIZATION OF TRANSONIC TURBINE VANES OPTIMIZED TO ATTENUATE ROTOR FORCING

R. Puente *

School of Aeronautics
Universidad Politécnica de Madrid
Madrid, 28040
Spain
Email: rpunterico@hotmail.com

G. Paniagua
T. Verstraete

Turbomachinery and Propulsion Department
von Kármán Institute for Fluid Dynamics
Rhode-Saint-Genése, B-1640
Belgium
Email: gpaniagua@me.com
verstraete@vki.ac.be

ABSTRACT

A multi-objective optimization procedure is applied to the 3D design of a transonic turbine vane row, considering efficiency and stator outlet pressure distortion, which is directly related to induced rotor forcing. The characteristic features that define different individuals along the Pareto Front are described, analyzing the differences between high efficiency airfoils and low interaction. Pressure distortion is assessed by means of a model that requires only of the computation the steady flow field in the domain of the stator. The reduction of aerodynamic rotor forcing is checked via unsteady multistage aerodynamic computations. A well known loss prediction method is used to drive the efficiency of one optimization run, while CFD analysis is used for another, in order to assess the reliability of both methods. In both cases, the decomposition of total losses is performed to quantify the influence on efficiency of reducing rotor forcing. Results show that when striving for efficiency, the rotor is affected by few, but intense shocks. On the other hand, when the objective is the minimization of distortion, multiple shocks will appear.

Keywords: rotor-stator interactions, shape optimization, transonic turbines, turbine vanes, performance predictions.

NOMENCLATURE

a	Sound speed
CL	Loss optimized geometry for the CFD driven optimization run
CU	Unsteadiness optimized geometry for the CFD driven optimization run
EPR	Events per revolution
HPT	High pressure turbine
H	Shape factor of a boundary layer
KL	Loss optimized geometry for the correlations driven optimization run
KU	Unsteadiness optimized geometry for the correlations driven optimization run
LE	Leading edge
LRS	Left running shock
LRS	Right running shock
\dot{m}	Mass flow
M_{is}	Isentropic Mach number
PS	Pressure side
p_s	Static pressure
p_0	Stagnation pressure
r	Radial coordinate
S	Shock function
SS	Suction side
TE	Trailing edge
T_0	Stagnation temperature

* Address all correspondence to this author.

\bar{u}	Velocity field
U	Resulting unsteadiness after integrating the forcing function over the risk region
Y	Stagnation pressure loss over outlet dynamic head
w	Coordinate of distance following the geometry of the leading edge of the rotor
α	Tangential flow angle
ψ	Forcing function according to the steady single row model
Ψ	Spectral decomposition of ψ
τ	Stagnation pressure loss over inlet stagnation pressure
θ	Angular coordinate for the pitchwise direction of a turbine
θ^*	Momentum thickness of a boundary layer

INTRODUCTION

The object of the present paper is the design and physical description of a high pressure turbine (HPT) vane operating in the transonic regime, which is aimed at reducing the interaction between rotor and stator, while preserving high efficiency. The main agent of row interaction is the shock system that develops at the trailing edge of an airfoil. In spite of the common belief that reducing shock intensity will mitigate both rotor forcing and losses, this paper illustrates the physics governing both contradictory effects.

The relevance of the study is based on the increasing importance of row interaction effects in aero-engine systems. Current design trends focus on weight and size reduction in order to improve the efficiency of the whole aircraft, which translates into reduced distance between components and a higher loading per stage. This results in an increased flow perturbation per row and less space for its damping, which according to Li and He [1, 2] can lead to forcing increments of 100 %. In order to tackle this problem, the inherent unsteadiness of the flow field should be taken into consideration in every stage of the design process (see Hodson *et al* [3]).

Turbomachinery flows are *per se* unsteady due to blade row rotation. Several unsteadiness sources have been identified, with comprehensive accounts found in Paniagua [4] and Payne [5]. These can be classified as pressure waves propagation or *potential effects*, viscous effects where convection of low momentum flow causes local pressure distortions, and shock waves. Supersonic flow is characterized by the limited attenuation of propagated perturbations. Therefore, the interaction between blade rows in transonic turbine stages will be of higher importance than in subsonic stages. Barter *et al* [6] investigated numerically the propagation of shocks across a stage, both considering and neglecting wave reflections between rows. Results showed that the stator's trailing edge shocks, when reflected from the rotor, do have an important impact on the vane's loading, but successive reflections back to the rotor pose an influence of second order.

Barter argues that only the unsteady frequency component corresponding to the first harmonic of the excitation is relevant. However, Kammerer and Abhari [7] demonstrate experimentally the importance of higher order harmonics.

Work on this topic has been carried out in the past at the Von Kármán Institute. Vascellari *et al* [8] identified theoretically the particularities of 2D profile velocity distributions that give rise to the trailing edge shock system. Joly *et al* [9] set as objective the minimization of vane outlet inhomogeneities using multi-objective optimization techniques, revealing efficiency and unsteady forcing are conflicting objectives. Multiple shock reflections may result in a reduced forcing at the expense of higher loss. Joly *et al* describe a geometry which achieves the same efficiency as a baseline one, while also minimizing the outlet pressure distortion. The pressure side is heavily modified, generating a narrower channel with a divergent passage. The sonic line shifts upstream and is more inclined, resulting in a larger acceleration at the pressure side, coupled with a straight suction side rear part. This results in a reduction of the pressure difference at the trailing edge.

The works previously mentioned were focused mainly in the study of 2D profiles. But this approach lacks applicability in low aspect ratio turbomachinery flows, which are highly three-dimensional. In annular cascades the radial distribution of specific mass flow is not uniform in general, so the same profile will not perform equally well at every radius. The effects of stacking law deviation with respect to the purely radial are summarized by Wang [10], where it is concluded that 2D design cannot be decoupled from 3D.

The novelty of this work can finally be stated as the identification of the 3D flow field features that distinguish between a low rotor forcing inducing HPT vane and a high efficiency one, and exploring the perspectives of improving both aspects.

OPTIMIZATION METHODOLOGY

In order to reduce rotor forcing by a traditional design method, several trial and error iterations would be necessary. By designing a geometry by means of an optimization method, access is directly granted to a well performing geometry which can be investigated at length. Provided that pressure distortion can be modeled, it can be set as the objective of such an optimization procedure. Maintaining a high efficiency will be a second objective.

An optimization problem consists of choosing the best solution amongst several possibilities. This statement can be mathematically formulated as the minimization of the so called objective functions, while taking into account constraining functions that need not be minimized but merely satisfied. The design space is the set of parameters that define the problem, which in practical situations vary within a bounded range.

The current problem is of a multi-objective nature. Gener-

ally, different objectives will enter into conflict with others. The solution will not be then a single geometry, but a set of geometries located in the so called Pareto Front. A set of designs is plotted in a graph whose axes correspond to the level of objective achievement, as shown in figure 4. Thus, the Pareto Front region can be defined as that in which no improvement towards an objective can be achieved without damaging another. The Pareto Front can also be thought of as the locus of the best geometries with varying objective priorities. By analyzing different solutions along the Pareto Front, insight can be provided upon the relationship between the different objectives.

The optimization code currently in use at the Von Kármán Institute is based on a Multi Objective Differential Evolutionary algorithm developed by Price and Storn [11]. Starting from an initial population, the performance of each individual is evaluated. Then, the whole population is sorted out by a ranking algorithm, and a new population is proposed according to a parameter modifying algorithm. The process is repeated for a specified number of *generations*.

GEOMETRY AND PHYSICS MODELING

Airfoil parametric definition

A three dimensional turbine airfoil is a complex geometry. While a well constructed optimization procedure requires the possibility of evaluating a wide variety of different geometries, a too large design space may render its solution infeasible. Another important issue is the linearity of the response of the objective function to different input design vectors. If a change of one parameter does not impact performance noticeably, the optimization problem will be ill-posed.

The strategy followed in the present work is that of parameterizing blade to blade sections, and applying a stacking law to build the full 3D blade. For the sake of simplicity, the meridional geometry will not be taken into consideration, although it is known that end-wall contouring can noticeably affect the pressure field [10].

Following the methodology proposed by Pierret [12], 2D sections are defined with a camberline, Suction Side (SS) and Pressure Side (PS) curves as depicted in figure 1a. The camberline is constructed via a Bézier curve by defining a control polygon. This is done by specifying the inlet, outlet and stagger angles, and an axial distance, namely the axial chord. This camber line is divided in several segments, applying a node stretching law. Normal to these nodes, at specified distances both above and below the camber line, are defined the control points that constitute the SS and PS curves. The last two control points of each side are linked by specifying wedge angles δ_{SS} and δ_{PS} . The TE is closed by a circular arc, and defines the position of the two last control points.

In this work three control sections will be parameterized. In total, 10 parameters define a profile: 4 control points for the SS,

3 for the PS, leading edge radius, and TE wedge angles. The inlet metal angle is imposed to be aligned with the inlet flow angle and the outlet metal angle is fixed at the desired outlet flow angle. Both axial chord and stagger angles are also fixed.

The stacking line is placed at the trailing edge in order to have higher control over final performance. The stacking law is then defined as the axial (sweep) and tangential (lean) displacement of the TE of each section with respect to the location of the TE of the hub profile (see figure 1b). To parameterize this stacking law, Bézier curves are again used, separating the effects of lean and sweep. At four equidistant radial stations (hub, tip and two other radii in between), the positions of the control points displacements are determined by the tip displacement, and the angles with the vertical at hub and tip (see figure 1c). Each stacking effect is determined with 3 parameters. In this paper only the effect of lean has been considered. A fixed number of airfoils is considered, so that every geometry has the same pitch spacing.

The three profiles and the stacking line add up to a total of 33 parameters to define a 3D airfoil.

Solver and mesh generation

Accurate CFD loss computation poses certain requirements, both in regards to mesh generation and flow modeling. Entropy generation mechanisms stem from viscous dissipation at small scales, either for laminar or turbulent flow. To resolve these phenomena, the mesh must be fine enough in the wall region, and must not introduce unphysical privileged propagation directions, for example, high aspect ratio or skewed cells misaligned with the flow.

TRAF is a flow solver developed by Arnone *et al* [13], which uses a Finite Volume spatial discretization and a Runge-Kutta type time integration scheme. Grid generation is performed through an automated procedure.

An implementation of the Baldwin-Lomax turbulence model is used, with no transition prediction capabilities. A fully turbulent boundary layer is assumed.

Boundary conditions and constraints

The boundary conditions of the vane are summarized in table 1. The inlet stagnation state is imposed as a constant radial distribution, both in the radial and circumferential directions. At the outlet, a circumferentially averaged radial distribution of static pressure is prescribed, which will be reached upon convergence. This boundary condition uses a static pressure value at hub, which is the one that corresponds to the specified M_{is} value, and a radial equilibrium calculation.

The postprocessing outlet plane is located where the rotor's LE is, that is, at $\frac{x}{c_{ax,hub}} = 0.4$ from the stator's TE. There, a restriction over outlet angle is formulated in Eqn. 1. This means that outside the boundary layer region, the outlet angle must match an objective distribution with a certain allowed error. This error

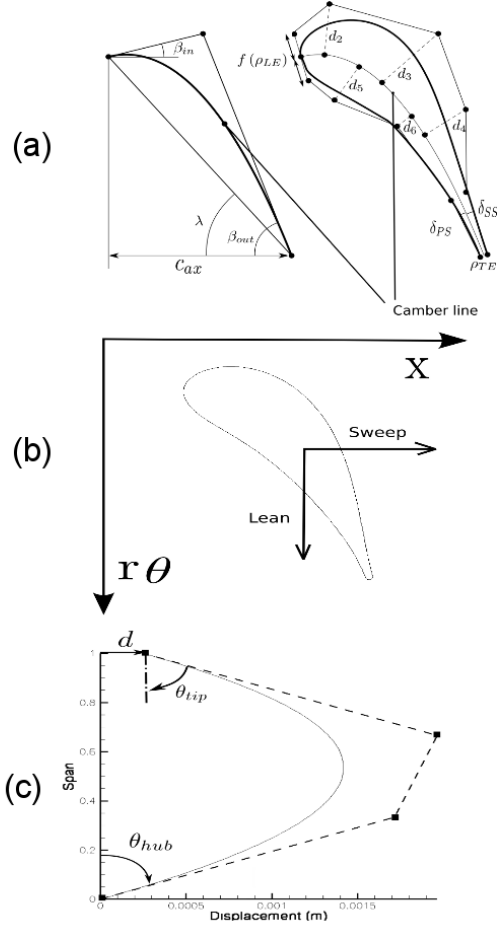


Figure 1: Blade parameterization

p_{01} (bar)	1.64
T_{01} ($^{\circ}$ K)	440
$M_{iS,2}$	1.25

Table 1: Boundary conditions

of 1.5° is high according to industry standards, but is allowed in order to be able to explore a wider design space. Given an outlet angle distribution and the previous boundary conditions, a nominal mass flow of $\dot{m} = 9 \text{ kg/s}$ is expected.

$$\Delta\alpha = \sqrt{\frac{1}{r_{80} - r_{20}} \int_{r_{20}}^{r_{80}} [\alpha(r) - \alpha_{obj}(r)]^2 dr} < 1.5^{\circ} \quad (1)$$

OBJECTIVES DEFINITION

Pressure distortion model

The ultimate aim of reducing unsteadiness is to prevent harmful structural vibrations. Methods do exist to compute the forced response of turbomachinery blades, but these require coupled fluid-structure multistage simulations, which can be either time resolved or linear harmonic decomposition methods, as used for example by Li and He [1] or by Escribano *et al* [14]. In either case, these calculations are very time consuming, thus infeasible to use in the context of an optimization procedure. A model which uses only steady computations on a single row is hereby proposed. Stemming from the assumption that the main component of rotor forcing is the non-uniformity of the pressure field induced by the stator, the objective will be the tailoring of the pressure distribution at a plane defined downstream of the stator in order to minimize the forcing on a given rotor geometry.

In a first approach, the rotor can be thought of as a body that traverses the non-homogeneous static pressure field left downstream by the stator. In its own reference frame, these inhomogeneities are felt like a time dependent inlet boundary condition. This situation is depicted in figure 2, for a rotor leaning in the sense of rotation, with \bar{w} denoting the direction of the rotor's stacking.

The proposed pressure distortion model translates all the information of the steady static pressure field at the stator's outlet into a time dependent global forcing function on the rotor. Eqn. 2 states the forcing function $\psi(\theta)$ as the averaging of the outlet pressure field in the direction of the rotor stacking, where w is the coordinate on a line parallel to the rotor's stacking line. Thus, $\psi(\theta)$ accounts for the total pressure forces felt by the rotor in terms of the pitchwise coordinate θ . This function is non-dimensionalized by the inlet total pressure.

The effect of the forcing function will be assessed by checking against a Campbell diagram. The first step is to transform $\psi(\theta)$ to the frequency domain by means of spectral analysis, as in Eqn. 3. The units there are the events per revolution (EPR). Then, each harmonic is represented in the diagram as a line that crosses the origin whose slope is the number of EPR. These lines will cross the eigenfrequency functions. The aim is to minimize the amplitude of the forcing function in a risk region bounded by the operating regime, the first eigenfrequency, and the last relevant eigenfrequency, as seen in figure 3. The order of this last eigenfrequency is particular for each rotor, being the sixth one in the case of the considered geometry.

Finally the unsteadiness function is defined in Eqn. 4. The integration limits allow the inclusion of the whole risk region. These limits are in this case $EPR_{min} = 9$ and $EPR_{max} = 59$.

Unsteady computations, performed with a Nonlinear Harmonic Method implemented in the commercial solver NUMECA FINE/Turbo [15], are carried out in order to compute the aerodynamic forcing. Thus, it can be checked whether rotor forcing is effectively reduced when minimizing pressure distortion.

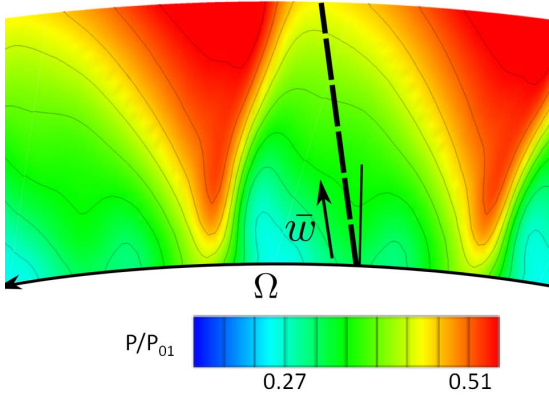


Figure 2: Rotor crossing a non-homogeneous pressure field

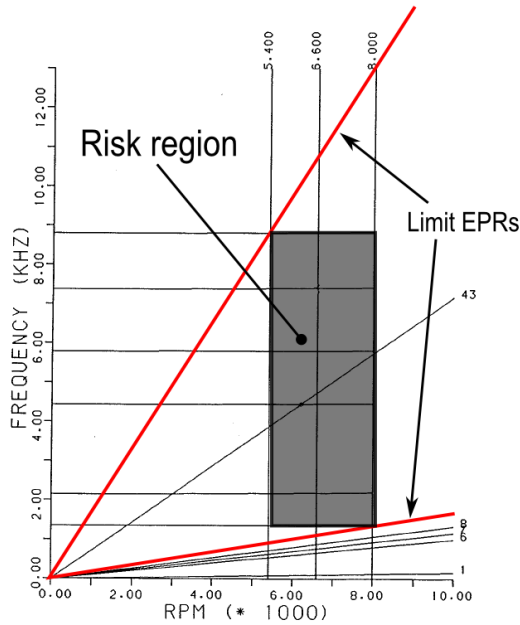


Figure 3: Campbell diagram of the considered rotor

$$\psi(\theta) = \frac{1}{w_{rip} - w_{hub}} \int_{w_{hub}}^{w_{rip}} \frac{p_s(\theta, w)}{p_{01}} dw \quad (2)$$

$$\Psi(EPR) = \int_{-\infty}^{\infty} [\psi(\theta) - \langle \psi(\theta) \rangle] e^{-ipEPR} d\theta \quad (3)$$

$$U = \sum_{EPR_{min}}^{EPR_{max}} \Psi(EPR_i) \quad (4)$$

Loss evaluation

Commercial CFD modeling made use of in this work has accuracy limitations. It might therefore be proposed to drive the loss objective by means of a performance prediction method based on correlations. This work will make use of a well known and widely used performance prediction method to assess loss levels, proposed by Kacker & Okapuu [16]. Loss is defined in terms of total pressure loss coefficient, as in Eqn. 5. This system is a mean line performance prediction method, which means that it must be fed values at midspan. The different mechanisms of loss generation are accounted for by adding up several loss components, as in Eqn. 6:

$$Y = \frac{P_{01} - P_{02}}{P_{02} - P_2} \quad (5)$$

$$Y_T = Y_p + Y_s + Y_{TET} + Y_{TC} \quad (6)$$

Y_p gathers the influence of midspan 2D geometry and flow field, Y_s accounts for the contribution of secondary flows, Y_{TET} provides with TE thickness (TET) blockage effects, and the term Y_{TC} means tip clearance losses. This last term will not be considered, as a vane does not have tip clearance.

This prediction system was developed from an experimental database of designs encompassing the state of the art in 1982, when only convergent passages and certain SS shapes were considered for transonic stages.

As the choice between working with correlations or relying solely in CFD is not obvious, in the present work the two methods are tested and compared. The flow field information needed by the correlations is extracted from CFD calculations which are needed anyway for the pressure distortion model. The geometric information is provided by the geometry generation software.

RESULTS AND DISCUSSION

The optimization runs were set for a population of 40 individuals, the initial one being a random set. Figure 4 shows the results of both runs, one whose efficiency objectives are driven by correlations and the other by pure CFD analysis. It can be seen how both loss computation methods are not wholly consistent with each other. Each run minimizes the loss according to the performance model used. Four geometries have been selected for further analysis, corresponding to the extremes of each Pareto Front. KL corresponds to the most efficient for the correlation driven run (K stands for Kacker & Okapuu), KU to the less forcing inducing. CL and CU are the analogous individuals for the CFD driven run. Note how not only Y is higher according to the CFD, but also the differences between maximum and minimum values. Note that correlations miss important geometrical information, as they assign similar performance values to

KU and CU, which are in fact very different as it will be shown in following sections.

$$\tau(\bar{x}) = \frac{p_{01} - p_0(\bar{x})}{p_{01}} \quad (8)$$

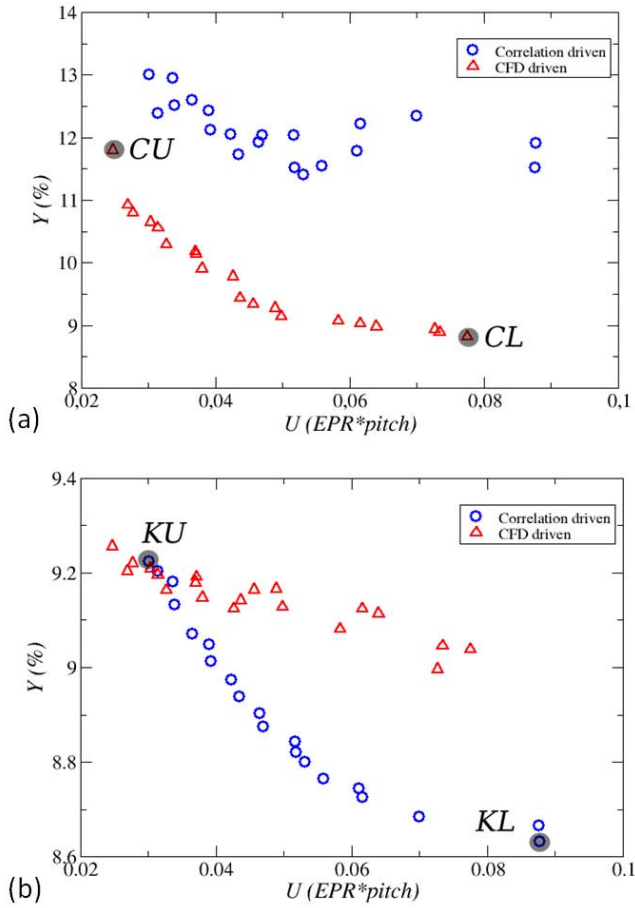


Figure 4: Pareto Fronts. Above, CFD computed efficiency. Below, correlation computed efficiency

Let us introduce two relevant variable fields, the Shock Function (see Eqn. 7) and the inlet based loss coefficient (see Eqn. 8). S is a scalar field which is positive in compression areas, above one in presence of shock waves, negative in expansion areas, and below one in expansion fans. Coefficient τ is appropriate for visualization purposes, as the non-dimensionalizing magnitude will be consistently the same for each analyzed geometry. These variables allow one to identify and characterize the observed shock structures, linking them directly to boundary layer loss generation mechanisms.

$$S(\bar{x}) = \frac{\bar{u}(\bar{x}) \cdot \nabla p(\bar{x})}{a(\bar{x}) |\nabla p(\bar{x})|} \quad (7)$$

Flow analysis at 10%, 50% and 90% span

Figure 5 presents flow channel geometries at the hub. The reduced thickness for both KU and KL is immediately apparent. Both SSs have an inflection point which likens the shape to that of a spike type supersonic nozzle. The Shock Function contours reveal compression waves emerging from the SS that eventually merge into Left Running Shocks (LRSs). From the PS at the TE, a Right Running Shock (RRS) emerges and impinges into the SS of the adjacent vane. This shock is reflected weakly in a region of expansion waves, so it is smothered and does not reach the postprocessing plane, indicated by the vertical black line. The black lines ($M_{is} = 1$ isolines) denote the throat line and enclose supersonic flow pockets in otherwise subsonic flow regions. The throat in KU is located slightly upstream compared to KL. CL and CU have a more conventional channel area distribution, leading to thinner airfoils, but the TE shock system deviates from conventional configurations. In CU the TE shocks are strong enough to allow both the LRS and the reflection of the RRS to reach the analysis plane. This occurs even though the reflected RRS is scattered in the wake, with one wave traveling downstream and another impinging again in the SS. In CL, both the reflected RRS and LRS are scattered in adjacent wakes, and their successive reflection creates a very complex shock pattern, but the ultimate outcome is that only one well defined shock arrives at the analysis plane. Again, the throat is shifted upstream for CU with respect to CL, but this time more noticeably. No separation occurs for either airfoil.

In the same vein, let us observe the midspan channel geometries in figure 6. A common feature is the presence of an inflection point, now in the PS of every airfoil. KL presents severe separation due to a PS concavity near the TE, correlations failed in this case to achieve good performance. It is seen how this concavity generates a train of compression waves that merge into a strong LRS that travels across wakes to reach the analysis plane. As at the hub, the RRS is weakened in an expansion region and extinguishes before reaching the rotor. In the case of KU there is no SS concavity, but slight separation takes place just upstream of the TE, as evidenced by the early emergence of the LRS. This is due to the difference between flow angle and metal angle at the TE, situation which is also found in other cases. The RRS is stronger than in KL and travels downstream across a wake, with a secondary scattered wave which dissipates when impinging again upon the SS. The CFD driven geometries do not show separation, nevertheless they present complex shock patterns. In CL, successive reflections of the RRS on the SS and the wake heavily affect the development of the LRS to the point that its

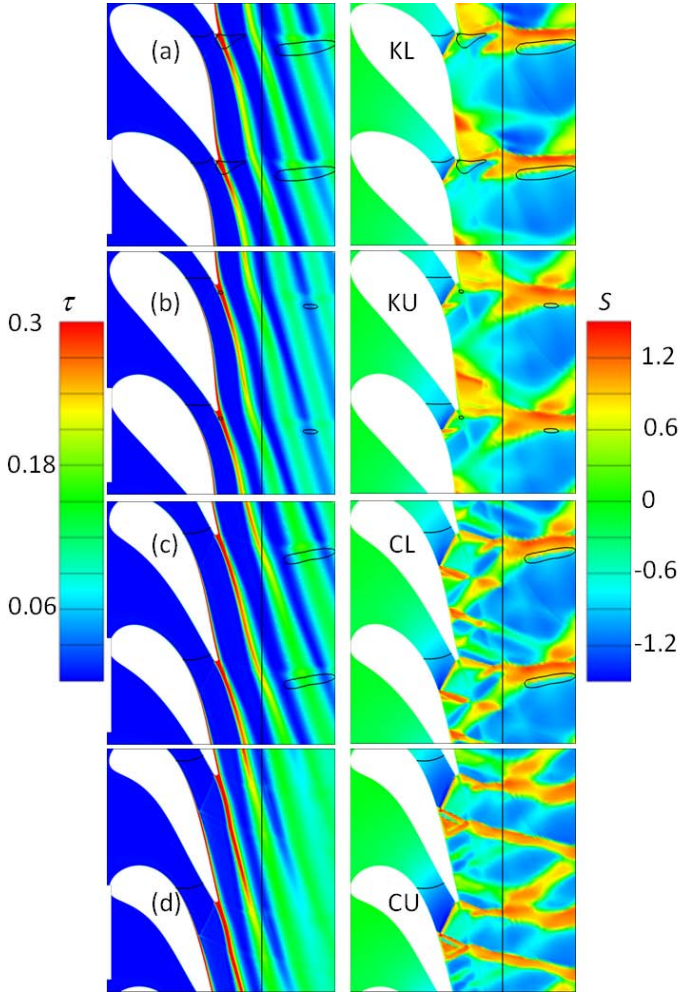


Figure 5: τ and S fields at hub

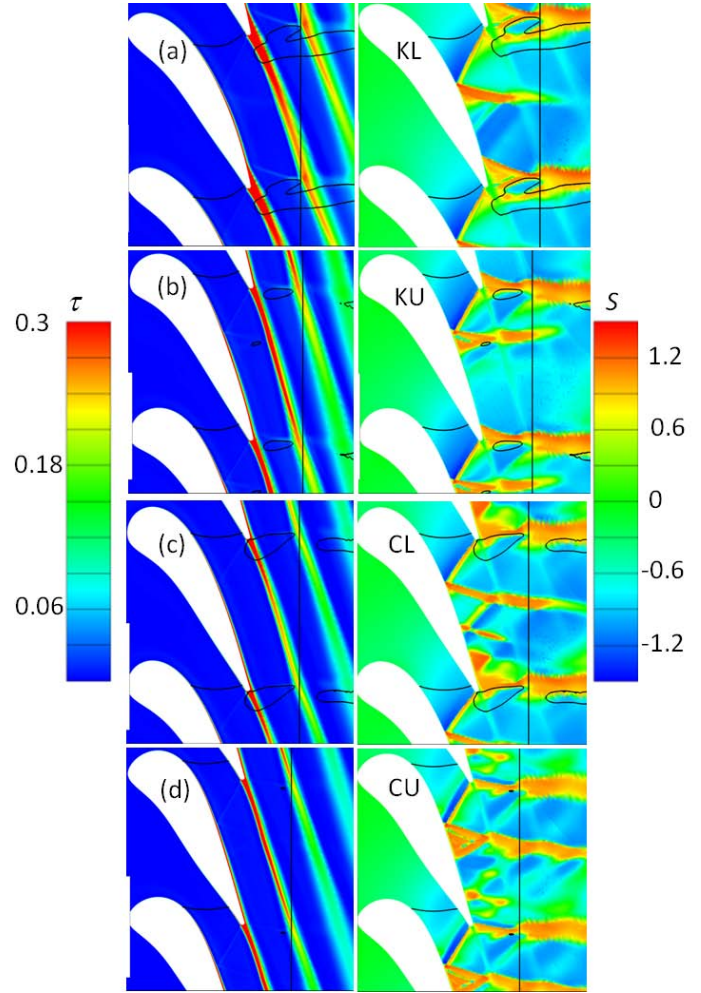


Figure 6: τ and S fields at midspan

origin is not well defined. The outcome is finally two strong shocks reaching the rotor. In CU, the situation is similar, but with one less SS shock reflection. Two weaker shocks reach the plane of interest. Now the upstream throat location shift is clear for both CU and KU.

At the tip, shock structures are simpler and no separation takes place for any geometry. The difference between outlet and metal angles causes an early rise of the LRS in KL and CL. The RRSs are particularly weak, not reaching the SS before becoming compression waves when weakened in accelerating flow. KU is a very conventional geometry, with well defined and strong LRS and RRS, the latter reflecting on the SS and traveling downstream. CU is similar in terms of flow field, if not in terms of geometry. It only adds a secondary scattered shock impinging on the SS, which does not reflect again. For the low forcing vanes, the movement of the throat takes place only in the SS, being attached to the TE at the PS. Again, for high efficiency vanes, one

strong shock reaches the rotor, whereas two weaker shocks do for the low forcing cases.

Outlet flow field and forcing analysis

Figure 8 shows a vane and the outlet static pressure field non dimensionalized by the inlet total pressure. For the efficient vanes KL and CL, a high pressure region is apparent. Following the opposite direction of the rotor's sense of rotation, the pressure drops steadily until it rises suddenly. This is particularly clear in Figure 9, where a shock column signals the abrupt rise, with compression appendages penetrating into low pressure regions. In KU, although a secondary shock column after the main can be noticed, the situation can be considered topologically the same, but the difference between maximum and minimum value is smaller and the pressure drop is less steep. In CU, two high pressure regions and their respective low pressure regions are

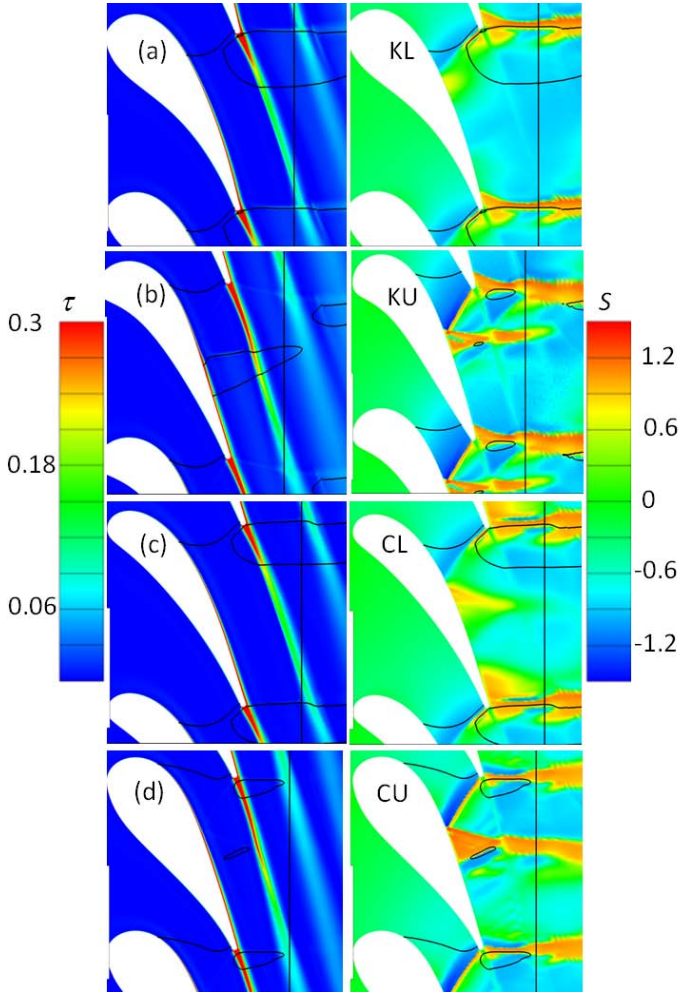


Figure 7: τ and S fields at tip

present, limited by corresponding shock columns.

These pressure fields translate into the forcing function models shown in figure 10a, and their spectral decomposition in figure 11a. KL, KU and CL share the same tendency in decreasing amplitude for higher order harmonics, but differing in magnitude. CU on the other hand presents a second harmonic which is stronger than the first. The same results are presented for the computed aerodynamic forcing in figures 10b and 11b. In order to present these data, the static pressure field over the rotor blades is extracted for 20 time steps per stator pitch from the unsteady multirow computations carried out with NUMECA FINE/Turbo. The resultant of the force is computed, and non dimensionalized by the rotor's area and the total inlet pressure. The forcing function follows the trend of the computed aerodynamic forcing for all cases except for KU, for which the second harmonic is greater than expected. But the first harmonic, the most dangerous in this case, is effectively smaller than for KL, its counterpart in the cor-

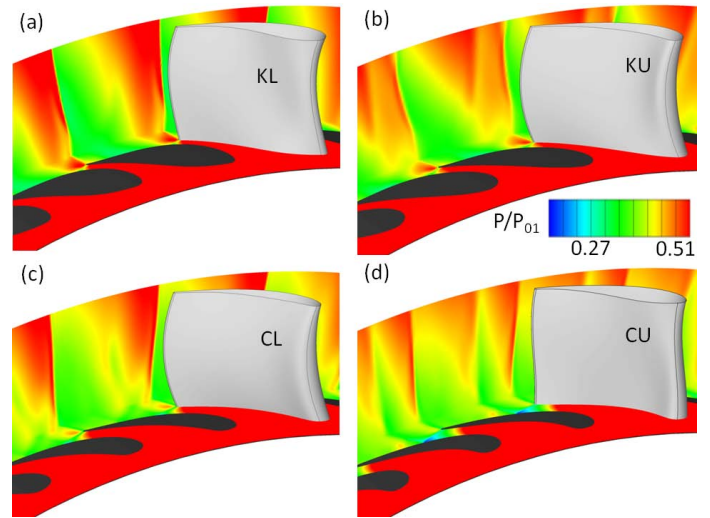


Figure 8: Outlet $\frac{P_s}{P_{01}}$ field

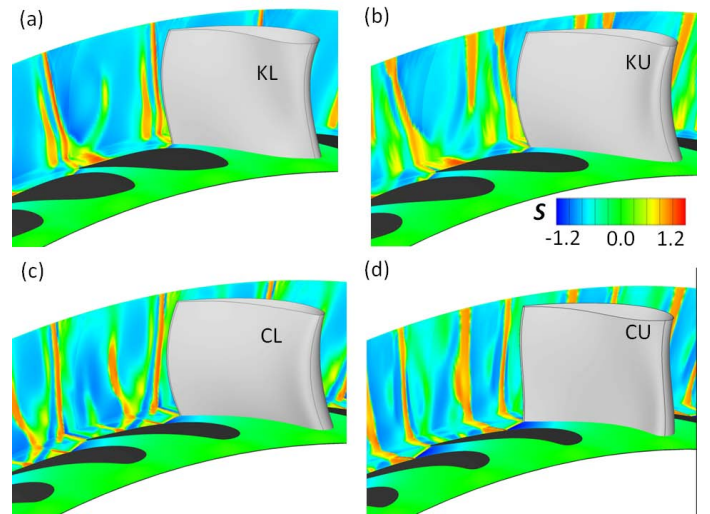


Figure 9: Outlet S field

relation driven run. The reason for the failure of the model in this case can be found in figures 5b and 6b. There are shock reflections that occur beyond the postprocessing plane that add further smoothing to the pressure field, but that could not take place, as the rotor has already disrupted them.

Making the analogy that the rotor is a moving object that encounters obstacles on its way, it is interesting to see what can be their size, number and how difficult they are to surpass. For that matter, figure 12 shows the isosurfaces of $M_{is} = 1$, which are relatively easy to overcome, and $M_{is} = 1.4$, more difficult. A translucent plane represents again the potential location of the rotor's LE. In KL and CL, the higher speed flow regions are con-

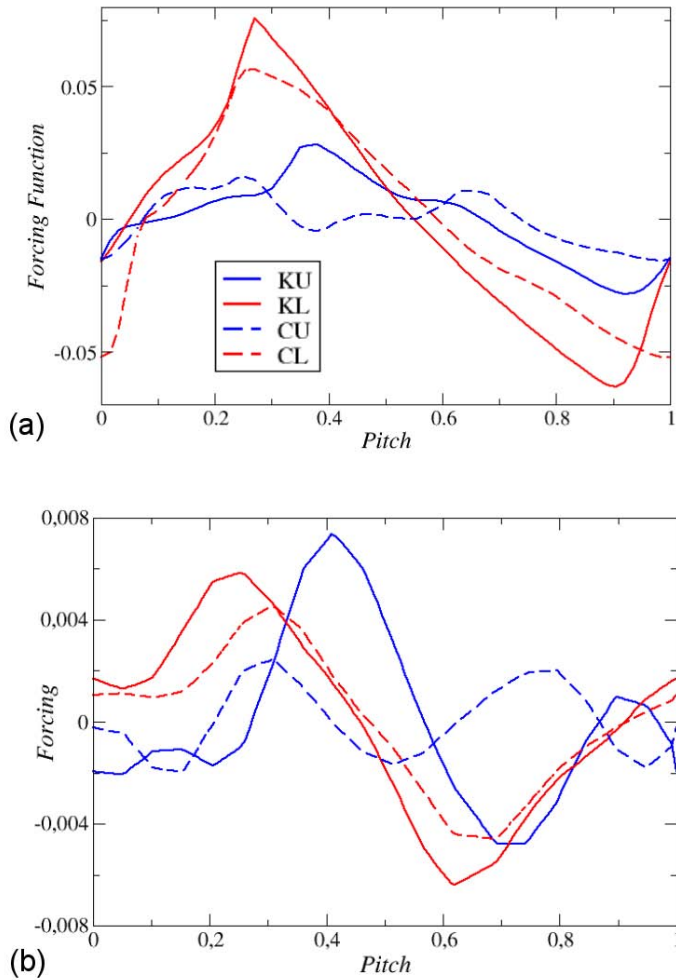


Figure 10: Forcing functions, spatial domain. Above, model function. Below, computed unsteady forcing

tained in pockets attached to the SSs behind the throat, and never threaten the rotor. However, supersonic flow is still contained within the large $M_{is} = 1$ structures, influencing the rotor along most of the span. In KU, the $M_{is} = 1.4$ region is larger, but remains harmless. Now the sonic surface only intercepts the rotor at the tip region. In CU, the red surfaces are largest, but again, they do not pose a threat. The influence of the blue surface is felt in a more extended region than in KU, but very slightly.

Figure 13 displays the isentropic Mach number distributions at 10%, 50% and 90% span. At the hub, the vanes are very aft loaded, which reduces the driving force of the passage vortex there. The airfoils are heavily unloaded here. For midspan and tip, efficient airfoils accelerate greatly in the vicinity of the LE, they reduce the acceleration and increase it again before the shock. Eqn. 9 [17] gives a measure of the growth of a 2D compressible boundary layer with traveled distance, and is given

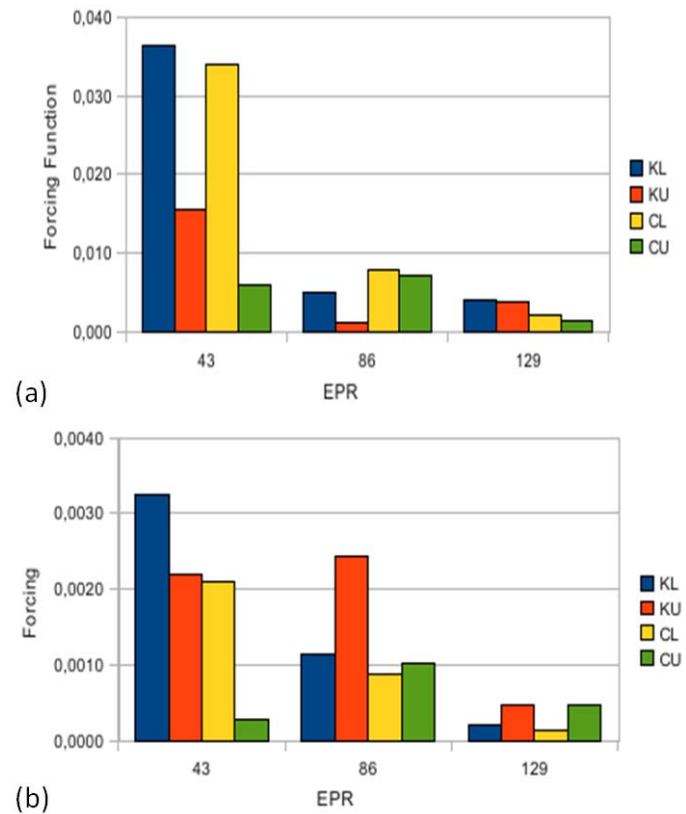


Figure 11: Forcing functions, spectral domain. Above, model function. Below, computed unsteady forcing

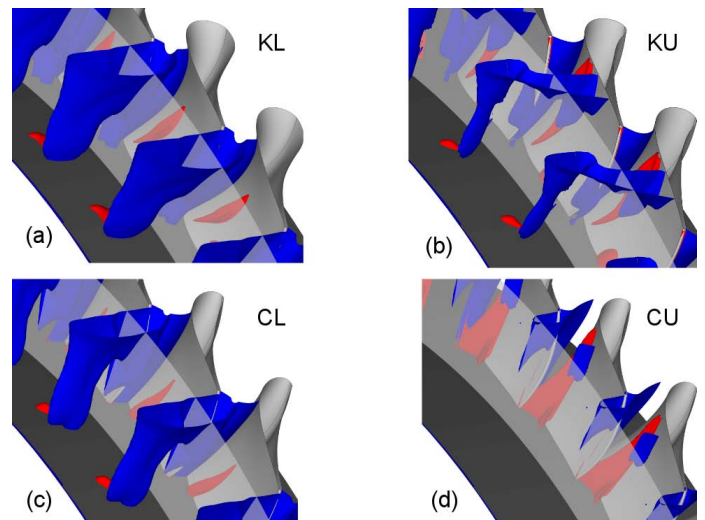


Figure 12: Isosurfaces of $M_{is} = 1$ (blue) and $M_{is} = 1.4$ (red)

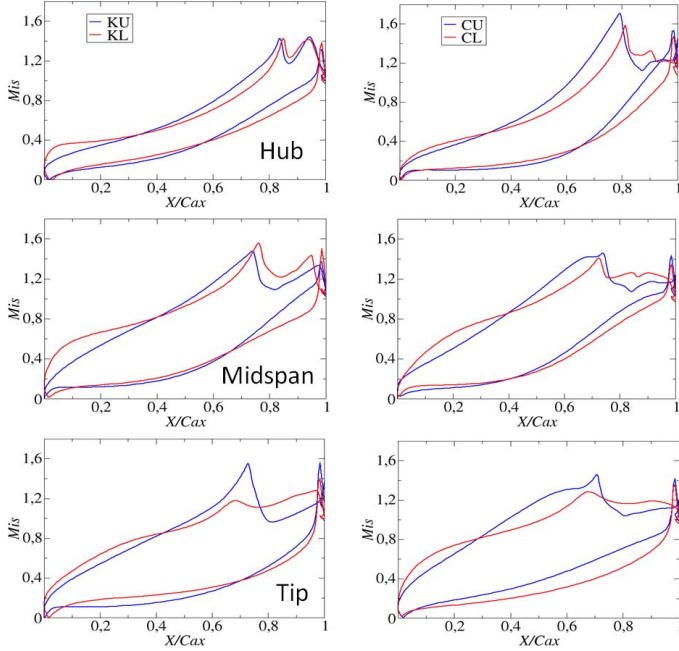


Figure 13: Descending: hub, midspan, and tip M_{is} distributions

for illustrative purposes. It shows that the momentum thickness grows proportionately to itself, flow acceleration and free stream Mach number. The growth is contained by a term proportional again to itself and acceleration, but modulated by the shape factor H , which in turn, grows with the square of the free stream Mach number, as found in Whitfield [18]. In efficient airfoils, strong acceleration is allowed at the beginning, while Me_e is still low. Then, acceleration is reduced until shortly before the impingement of the RRS, when it is strongly enforced to mitigate the growth of the boundary layer. Low forcing airfoils have a relatively constant flow acceleration, and the drop after the SS shock leaves a lower velocity than for efficient airfoils. Regarding the PSs, efficient vanes reach lower velocities, thus having a greater difference between SS and PS. At midspan, the concavity of PS near the TE, reduces the acceleration, and the total effect is akin to that of a supersonic nozzle that tries to achieve uniform outlet conditions.

$$\frac{d\theta^*}{dx} = c_f(x) + [M_e^2 - H(x) - 2] \frac{\theta^*}{u_e} \frac{du_e}{dx} \quad (9)$$

Loss decomposition and circumferentially averaged analysis

In Table 2 a relation of each loss component is found for each geometry, calculated with correlations. The secondary loss components do not vary, which is confirmed by the CFD computed spanwise distributions in Figure 14b for all geometries except for CU. This geometry has heavy secondary losses at hub, which is not predicted by the correlations, due to an increased loading with respect to its efficient counterpart CL. The passage vortices at hub and tip cause underturning (see Figure 14a), and a local secondary loss decrease. The general tendency is a decrease of loss with going up along the span, which is consistent with both the outlet angle tendency and the massflow distribution. The separated flow present for the correlation driven run at midspan disrupts, but does not invalidate this description. The inlet massflow, pictured in Figure 14c, shows how blockage decreases along the span for all geometries and how the efficient vanes achieve a higher massflow due to a lower average outlet angle. According to the correlations, the difference in efficiency is due to the influence of both profile losses and throat blockage, which is this time fully confirmed qualitatively by CFD, as was seen during the previous analysis of throat sections. A summary of the CFD predicted performances are provided in Table 3.

	KL	KU	CL	CU
$Y_p(\%)$	2.62	2.93	2.88	2.89
$Y_s(\%)$	5.39	5.38	5.39	5.39
$Y_{TET}(\%)$	0.61	0.89	0.75	0.99
$Y_T(\%)$	8.63	9.22	9.03	9.25

Table 2: Loss decomposition

	KL	KU	CL	CU
$Y(\%)$	12.03	13.01	8.81	11.79
$\dot{m}(kg/s)$	11.25	9.84	11.41	10.16
Objective mass flow deviation (%)	25	9.3	26.78	12.89

Table 3: Computationally predicted performance

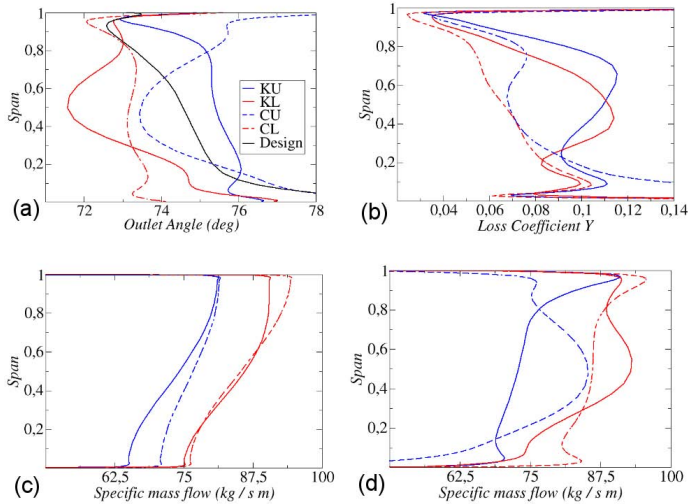


Figure 14: Circumferentially averaged radial distributions

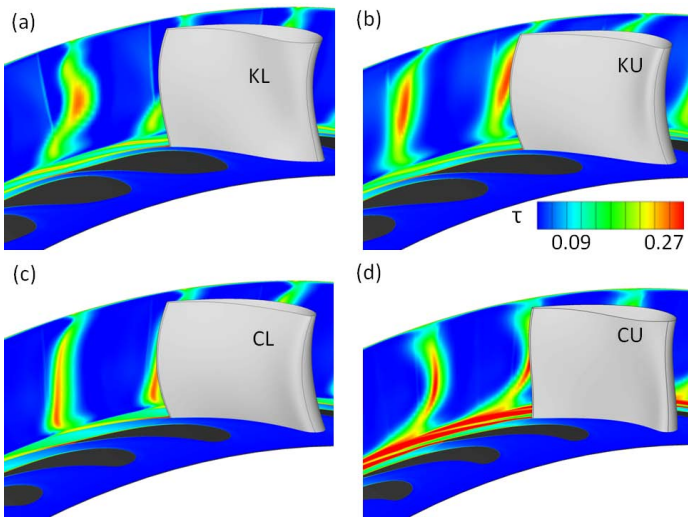


Figure 15: Outlet τ field

Stacking line effect

All KU, KL and CL exhibit a compound lean, being monotonously concave at the SS. This configuration decreases the pressure gradient between SS and PS at the endwalls, thus reducing the secondary losses. CU, on the other hand has a double compound lean with a convexity at hub that increases said pressure gradient, and explains the high secondary losses there. But this increased pressure gradient helps in the development of the strong shocks that characterize this geometry. In Figure 15, it is seen that the loss field follows the lean.

CONCLUSIONS

Firstly, a model of unsteady pressure excitations which requires only the steady computation of the upstream row is presented. This model is physically sound and has been validated against unsteady multirow computations, which are one order of magnitude higher in terms of computational expense. However, special care must be taken when defining the computational domain. The outlet plane should be same as the postprocessing plane, located at the axial position of the leading edge of the downstream row.

Secondly, the performance of both CFD loss computations and a correlation based performance prediction system has been compared. Even though CFD may not be quantitatively accurate, it is better suited for finding the location of the optima, as it is based on physics. Correlations failed in general terms to deliver optimal characteristics, so their use would need further restrictions on geometry, such as airfoil thickness and curvature, or performance, forbidding separation.

Finally, these tools have been used to generate well performing turbine geometries in terms of induced rotor forcing and efficiency. Selected geometries from the extreme points of the Pareto Fronts of two optimization runs show how efficiency is lost while reducing rotor forcing. These geometries are analyzed and the relevant flow features, such as shock systems and interaction between shocks and viscous flow, are identified and described. Rotor forcing is reduced by smoothing the static pressure field by means of increasing the number and reducing the intensity of shocks. The conclusion is that a great potential for rotor excitation reduction exists while still achieving high efficiency.

ACKNOWLEDGMENT

The authors would like to acknowledge the help provided by J. Prinsier and Z. Alsalihi by carrying out the unsteady multirow simulations and helping with the postprocessing. This work has also benefited greatly from the assistance of M. Joly through his know-how, and the insight gained during his previous work.

REFERENCES

- [1] H. D. Li, L. He, 2005. "Blade aerodynamic damping variation with rotor-stator gap: A computational study using single-passage approach". *Journal of Turbomachinery*, **127**, pp. 573–579.
- [2] H. D. Li, L. He, 2005. "Towards intra-row gap optimization for one and a half stagetransonic compressor". *Journal of Turbomachinery*, **127**, pp. 589–598.
- [3] H. P. Hodson, T. P. Hynes, E. M. Greitzer, C. S. Tan, 2009. "A physical interpretation of stagnation pressure and enthalpy changes in unsteady flow". In Proceedings of the ASME TurboExpo.

- [4] Paniagua, G., 2002. “Investigation of the steady and unsteady performance of a transonic hp turbine”. PhD thesis, Université Libre de Bruxelles.
- [5] S. J. Payne, 2001. “Unsteady loss in a high pressure turbine stage”. PhD thesis, University of Oxford.
- [6] J. W. Barter, J. P. Chen, P. H. Vitt, 2000. “Interaction effects in a transonic turbine stage”. In Proceedings of the ASME TurboExpo, ASME, ed., Vol. 2000-GT-0376.
- [7] A. Kammerer, R. S. Abhari, 2009. “Blade forcing function and aerodynamic work measurements in a high speed centrifugal compressor with inlet distortion”. In Proceedings of the ASME TurboExpo.
- [8] M. Vascellari, R. Dénos, R. Van den Braembussche, 2004. “Design of a transonic high-pressure turbine stage 2d section with reduced rotor/stator interaction”. In Proceedings of the ASME TurboExpo, ASME, ed., Vol. GT2004-53520.
- [9] M. Joly, T. Verstraete, G. Paniagua, 2010. “Attenuation of vane distortion in a transonic turbine using optimization strategies”. In Proceedings of the ASME TurboExpo, ASME, ed., Vol. GT2010-22370.
- [10] Wang, Z., 1999. Three-dimensional theory and design method of bowed-twisted blade and its application to turbomachines. “Turbomachinery Blade Design Systems”, VKI Lecture Series.
- [11] K. Price, N. Storn, 1997. Differential evolution- a simple and efficient adaptive scheme for global optimization over continuous spaces. Tech. Rep. TR-95-012, University of California.
- [12] Pierret, S., 1999. “Designing turbomachinery blades by means of the function approximation concept based on artificial neural network, genetic algorithm, and the navier stokes equations”. PhD thesis, Faculté Polytechnique de Mons.
- [13] A. Arnone, M. S. Liou, L. A. Povinelli, 1995. “Integration of navier-stokes equations using dual time stepping and a multigrid method”. *AIAA*, **33**, pp. 985–990.
- [14] A. G. Escribano, A. Serrano, C. Vasco, 2003. “Cascade-gust interaction problem analysis based on linear cfd calculations”. In 4th CAA Workshop on Benchmark Problems.
- [15] Wilquem, F., 2008. *FINE Turbo v8 Manual: Unsteady Treatment, Non-Linear Harmonic Method*. NUMECA International.
- [16] S. C. Kacker, U. Okapuu, 1982. “A mean line prediction method for axial flow turbine efficiency”. *Journal of Engineering for Power*, **104**, pp. 111–119.
- [17] de la Calzada, P., 2003. “Low pressure turbine design”. In Aero Engine Design: A State of the Art, VKI Lecture Series, V. K. Institute, ed.
- [18] Whitfield, D. L. Integral solution of compressible turbulent boundary layers using improved velocity profiles. Tech. Rep. AEDC-TR-78-42, Arnold Engineering Development Center.